Available online at www.sciencedirect.com
SCIENCE DIRECT®
Journal of Catalysis 227 (2004) 419–427
JOURNAL OF CATALYSIS
www.elsevier.com/locate/jcat

Mesoporous silica-supported Ni–B amorphous alloy catalysts for selective hydrogenation of 2-ethylanthraquinone

Xueying Chen, Shuai Wang, Jihua Zhuang, Minghua Qiao *, Kangnian Fan, Heyong He *

Department of Chemistry and Shanghai Key Laboratory of Molecular Catalysis and Innovative Materials, Fudan University, Shanghai 200433, People's Republic of China

Received 21 April 2004; revised 23 June 2004; accepted 5 August 2004

Abstract

The effects of pore structure on the reaction rates and selectivities in the liquid-phase hydrogenation of 2-ethylanthraquinone over Ni–B amorphous alloy catalysts prepared by the reductant-impregnation method were studied using regular (HMS, MCM-41, and SBA-15) and commercial mesoporous silicas as supports. The composition, particle size, and location of the Ni–B particles were profoundly influenced by the pore structure of the supports. It is found that the location of the Ni–B particles depended on the pore size of the supports, whereas the uniformity of particle size was related to the interaction between the Ni–B particles and the supports. The hydrogenation rate was much faster on Ni–B catalysts with pore diameters exceeding 5 nm than on the narrow-pore catalysts, whereas the selectivity to 2-ethyldihydroanthraquinone, the carbonyl group hydrogenation product, was higher on Ni–B catalysts supported on regular mesoporous silicas. The best activity and selectivity were achieved when using SBA-15 as the support, which is attributable to the formation of more uniform active sites due to the unique pore structure of SBA-15.

Keywords: Ni–B amorphous alloy; Mesoporous silica; 2-Ethylanthraquinone; Hydrogenation; H_2O_2

1. Introduction

Discovered by Thenard in 1818, H_2O_2 has been widely used in textile bleaching and to prepare other peroxides [1–3]. Since the only by-product formed is water, H_2O_2 is often referred to as "friendly" oxidant. Although there are many ways to produce H_2O_2, by far the dominating process is the anthraquinone autoxidation process [1–3]. In this famous process (Scheme 1), 2-ethylanthraquinone (eAQ) dissolved in a suitable solvent (working solution) is cycled between two main steps:

(1) eAQ in the working solution is hydrogenated catalytically to the corresponding "active quinones" ($eAQH_2$ and H_4eAQH_2);
(2) The "active quinones" are oxidized with an oxygen-containing gas to produce H_2O_2 and simultaneously recover eAQ and H_4eAQ.

Further details of this process can be found in Refs. [1–3]. Note that to maintain the cycle, a very high overall selectivity to "active quinones" (well above 99%) is required. So the catalyst used in the hydrogenation step should be highly selective. In industry, Raney Ni and palladium are the most commonly used catalysts for this reaction. However, even on the most selective palladium catalyst, during the hydrogenation step eAQ can be deep hydrogenated to some degradation products such as H_8eAQH_2, 2-ethylanthracene (eAT), and 2-ethylanthrone (eAN) [4,5]. Such degradation products cannot be oxidized to produce H_2O_2, thus leading to the loss of the expensive anthraquinones and fed hydrogen. On the other hand, the oxidation rate of H_4eAQH_2 is remarkably slowed down as compared to $eAQH_2$, leading to lower efficiency in H_2O_2 production [6]. Thus it is highly desirable if

---

* Corresponding authors. Fax: (+86-21) 65642978.
E-mail addresses: mhqiao@fudan.edu.cn (M.H. Qiao), heyonghe@fudan.edu.cn (H.Y. He).

0021-9517/$ – see front matter © 2004 Elsevier Inc. All rights reserved.
doi:10.1016/j.jcat.2004.08.002

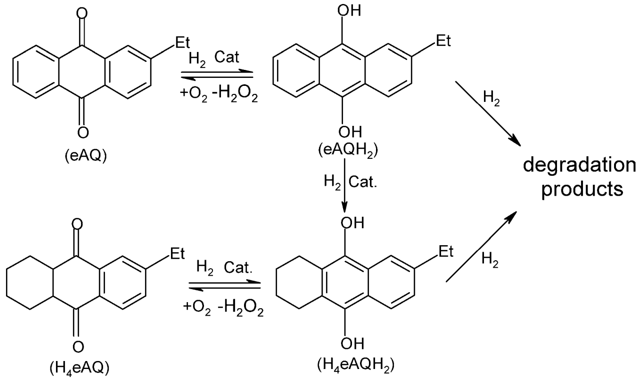

Scheme 1.

one can develop a catalyst exhibiting exclusive selectivity to $eAQH_2$ rather than to H_4eAQH_2; i.e., the catalyst is exclusively selective in hydrogenating the carbonyl group rather than the aromatic ring.

Recently, amorphous alloy catalysts with short-range ordering and long-range disordering structure have attracted much attention owing to their special physical and chemical properties such as unique isotropic structure and high concentration of coordinatively unsaturated sites [7–9]. Industrial application of those amorphous alloy catalysts is limited, however, due to their low surface area and poor thermal stability. One of the most promising ways to overcome those drawbacks is to deposit them on a support with high surface area. The supported amorphous alloy catalysts have been shown to be of better thermal stability than the corresponding unsupported amorphous ones, higher activity and selectivity than the crystalline counterparts, and less pollution than the Raney metal catalysts [10–14].

Regular mesoporous molecular sieves have shown great potential in catalysis, which is closely related to their specific features such as extremely high surface area and narrow pore-size distribution [15]. Their large channels allow diffusion of bulky compounds and present different types of shape selectivity such as reactant, product, and transition state. These unique features of mesoporous molecular sieves offer new possibilities for obtaining highly dispersed metal catalysts and motivate us to study nickel boride amorphous alloy catalyst supported on mesoporous molecular sieves.

In a recent research note, we have briefly reported the excellent selectivity of the SBA-15-supported amorphous nickel boride alloy catalyst in eAQ hydrogenation to $eAQH_2$ [16]. This paper addresses the effects of pore structure on the composition, size, and distribution of the Ni–B particles and catalytic behavior in eAQ hydrogenation of amorphous Ni–B catalysts supported by mesoporous silicas. Both regular and commercial mesoporous silicas were used as catalyst supports. Inductively coupled plasma-atomic emission spectroscopy (ICP-AES), nitrogen physisorption, X-ray diffraction (XRD), transmission electron microscopy (TEM), X-ray photoelectron spectroscopy (XPS), and H_2 chemisorption were used to characterize the catalysts and the different catalytic behaviors were correlated.

2. Experimental

2.1. Catalyst preparation

Pure siliceous SBA-15, MCM-41, and HMS mesoporous molecular sieves were synthesized according to the well-established procedures [17–19] and a commercial mesoporous silica was obtained from Qingdao Haiyang Chemical Corp. All silicas were crushed and sieved to a particle size of 40–60 mesh.

The amorphous Ni–B particles were introduced to silicas by a reductant-impregnation method described as follows. The silica (1.0 g, 40–60 mesh) was first immersed into the potassium borohydride solution (3.0 M, 13.74 mmol) for 15 min, then the excessive solution was removed. Reduction commenced as soon as the nickel chloride solution (0.42 M, 3.41 mmol) was added to the borohydride-impregnated support. The mixture was placed undisturbedly until no bubbles were generated. The resulting black catalyst was washed with distilled water to neutrality, and then with ethanol three times to replace water. The catalyst was finally kept in ethanol for characterization and prior to activity test.

The Raney Ni catalyst (Degussa) was used for comparison. Since all catalysts can be oxidized easily, great care must be taken to avoid their exposure to air.

2.2. Characterization

The bulk compositions of the as-prepared catalysts were determined by ICP-AES (Thermo Elemental IRIS Intrepid).

The Brunauer–Emmett–Teller surface areas (S_{BET}) and pore-size distribution (PSD) of mesoporous silicas were measured using N_2 physisorption at 77 K. Prior to measurement, samples were transferred to the glass adsorption tube and degassed at 383 K under ultrahigh pure nitrogen flow for 2.0 h. The nitrogen adsorption–desorption isotherms were acquired on the Micromeritics TriStar 3000 apparatus. The pore volume was calculated from the amount of N_2 adsorbed at a relative pressure of 0.995. The pore-size distribution curves were calculated from the desorption branches of the isotherms using Barrett–Joyner–Halenda (BJH) formula [20].

The pore structure and the Ni–B particle size of the as-prepared catalysts were observed by TEM (JEOL JEM2011) fitted with an energy-dispersive X-ray emission analyzer (EDX) with mapping facility. The amorphous character of the catalysts was verified by selected-area electron diffraction (SAED).

The XRD patterns were collected on a Bruker AXS D8 Advance X-ray diffractometer using Cu-Kα radiation ($\lambda = 0.15418$ nm). The tube voltage and current was 40 kV and 40 mA, respectively. Catalyst with solvent was put on the sample stage, with argon flow (99.9995%, deoxygenated by an Alltech Oxy-trap filter) purging the sample during the detection to avoid oxidation. Crystallization of the catalyst was monitored in situ by elevating the stage temperature from room temperature to 873 K.

The active surface area was measured by pulsed H_2 chemisorption, assuming $H/Ni(s) = 1$ and a surface area of 6.5×10^{-20} m^2 per Ni atom [21]. Turnover frequency (TOF) was expressed as the number of H_2 molecules consumed per active surface nickel atom per second by differentiating the H_2 uptake curve and extrapolating to the zero reaction time.

The types of adsorption sites existing on the catalyst were studied by temperature-programmed desorption of H_2 (H_2-TPD). After the sample was treated at 473 K for 2.0 h under argon flow (99.9995%, deoxygenated by an Alltech Oxytrap filter), it was cooled down to room temperature followed by being exposed in deoxygenated H_2 for 1.0 h to ensure the saturation adsorption of hydrogen. The catalyst was then purged with argon to remove gaseous and/or physisorbed hydrogen. The maximum desorption temperature, 873 K, was reached at a ramping rate of 20 $K\,min^{-1}$. The H_2 signal (mass 2) was monitored by an on-line mass spectrometer (MS, SRS 200).

The surface composition and electronic state of the catalyst were detected by XPS (Perkin Elmer PHI 5000C). The spectra were recorded with Mg-Kα line as the excitation source ($h\upsilon = 1253.6$ eV). The sample was pressed to a self-supported disk and kept in ethanol before mounting on the sample plate. It was degassed in the pretreatment chamber at 383 K for 2 h in vacuo before being transferred into the analyzing chamber where the background pressure was better than 2×10^{-9} Torr. All the binding energy (BE) values were obtained after removing the surface oxides by Ar ion sputtering and referenced to the C 1s peak of contaminant carbon at 284.6 eV with an uncertainty of ± 0.2 eV.

2.3. Activity test and product analysis

The activity test was carried out in a 220-ml stainless-steel autoclave with a magnetic stirrer. A mixture of trioctylphosphate and trimethylbenzene (volume ratio 3/7) was used as the solvent and the concentration of eAQ in the working solution was 50 $g\,l^{-1}$. The reaction conditions were as follows: 70 ml of working solution, 1.0 g of catalyst, reaction temperature of 323 K, H_2 pressure of 0.3 MPa, and a stirring rate of 1000 rpm to exclude the diffusion effect.

The reaction process was monitored by sampling the reaction mixture at intervals for O_2 oxidation. The H_2O_2 produced was extracted by distilled water and then titrated by $KMnO_4$ in acidic solution. The percentage yield of H_2O_2 (X) is expressed as the ratio of the moles of H_2O_2 to the initial moles of eAQ in the reactor, i.e., $X = n^t_{H_2O_2}/n^0_{eAQ} \times 100\%$, which also represents the selectivity to $eAQH_2$ and H_4eAQH_2. The organic layer after H_2O_2 extraction was analyzed by high-performance liquid chromatography (HPLC, Hewlett-Packard HP1100) with an accuracy of 5%. eAQ and H_4eAQ can be readily quantified by HPLC with an ultraviolet detector employing the Zorbax column (ODS, 4.6 mm × 15 cm). It is found that under the present reaction condition only eAQ and H_4eAQ exist, as also confirmed by Finnigan Voyagen GC-MS equipped with HP-5 capillary column (30 m × 0.25 mm, 0.25 μm).

3. Results and discussion

3.1. Catalyst texture

The nitrogen adsorption–desorption isotherms and the corresponding pore-size distribution curves of the original mesoporous silicas are shown in Fig. 1a and 1b. The BET surface area, total pore volume, and average pore diameter are presented in Table 1. The BET surface area in all regular mesoporous silicas (SBA-15, HMS, and MCM-41) is higher than 750 $m^2\,g^{-1}$, whereas it is much lower for commercial SiO_2 (446.3 $m^2\,g^{-1}$). In Fig. 1a, the isotherms of SBA-15 and commercial SiO_2 show a type IV shape with type A hysteresis loop according to the classification

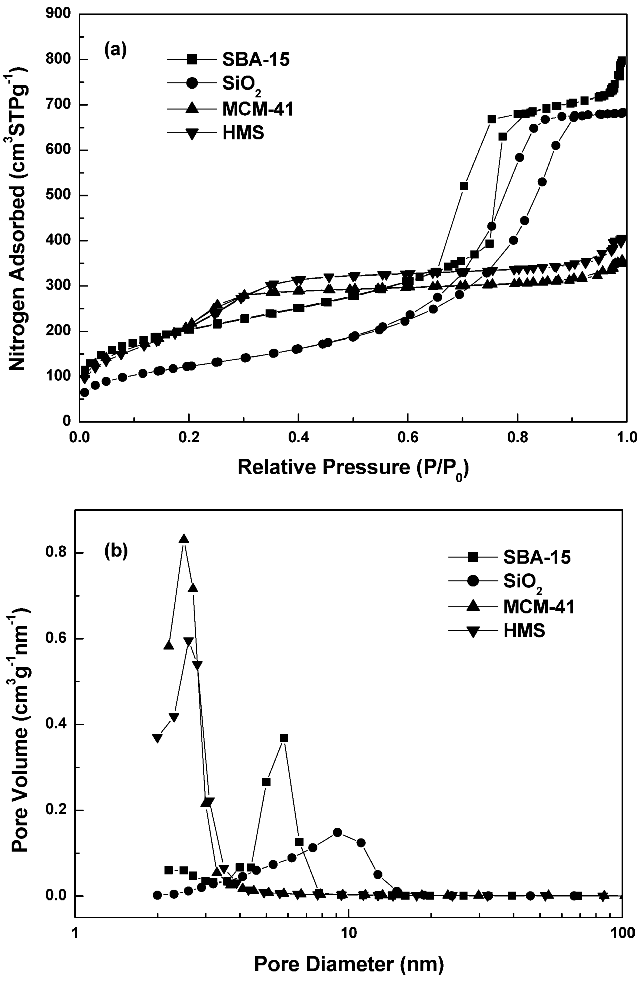

Fig. 1. Nitrogen adsorption–desorption isotherms (a) and pore-size distribution curves calculated by the BJH equation in the desorption branch (b) of siliceous SBA-15, MCM-41, HMS, and commercial SiO_2.

Table 1
Physicochemical properties of the mesoporous silica-supported Ni–B catalysts

Sample	Ni loading (wt%)	Composition (atomic ratio)	S_{BET} ($m^2\ g^{-1}$)	V_{pore} ($cm^3\ g^{-1}$)	d_{pore} (nm)	S_H ($m^2\ g_{Ni}^{-1}$)	$d_{Ni–B}$ (nm)
SiO_2	–	–	446.3	1.057	7.26	–	–
Ni–B/SiO_2	11.3	$Ni_{65.8}B_{34.2}$	440.2	0.918	5.87	8.7	10
HMS	–	–	779.8	0.628	3.22	–	–
Ni–B/HMS	11.9	$Ni_{48.8}B_{51.2}$	599.7	0.510	3.18	4.5	15
MCM-41	–	–	776.9	0.664	2.92	–	–
Ni–B/MCM-41	11.8	$Ni_{69.8}B_{30.2}$	542.3	0.582	2.88	5.1	50
SBA-15	–	–	767.6	1.223	6.48	–	–
Ni–B/SBA-15	9.8	$Ni_{57.7}B_{42.3}$	367.0	0.482	6.47	11.2	6

of IUPAC [22], indicating the presence of tubular pores of relatively large pore sizes. The much sharper inflection of the adsorption branch at P/P_0 in the range of 0.7–0.8 for SBA-15 confirms its high quality with uniform mesoporosity [23]. On the other hand, the shape of the isotherms of HMS and MCM-41 corresponds to the adsorption of N_2 on the walls of narrow mesopores. As expected, the BJH pore-size distribution curves (Fig. 1b) are narrower for regular mesoporous silicas than for commercial SiO_2, and the average pore diameters of SBA-15 and commercial SiO_2 are much larger than those of HMS and MCM-41 (also shown in Table 1).

Introduction of Ni–B does not change the preliminary lineshape of the isotherms, though Fig. 2a and 2b clearly evidence the decrease in both the total pore volume and average pore diameter of the mesoporous silicas to a more or less extent. It is noted that the pore-size distribution curves of SBA-15, MCM-41, and commercial SiO_2 presented in Fig. 2b exhibit an additional peak at ∼3.9 nm. Considering the pore size of SBA-15 and commercial SiO_2, at first sight one may attribute it to partial blocking of the large pores by Ni–B particles. However, this assumption cannot rationalize the case of Ni–B/MCM-41, since the “pore size” exceeds the pore diameter of original MCM-41 of 2.92 nm. The origin of the peak from Ni–B itself can also be ruled out, as in a separate experiment virtually no peak in the mesoporous region was found for unsupported Ni–B particles due to the nonporous texture of the amorphous Ni–B particles [8]. As a result, we assign the peak to an artifact reflecting the tensile strength effect of the adsorbate according to Gregg and Sing [24] and Khodakov et al. [25].

In Table 1, the most drastic decrement in total pore volume and BET surface area is found on Ni–B/SBA-15 catalysts: they are less than one-half of those of SBA-15, whereas the decrement is ∼30% at most for other catalysts. This phenomenon strongly suggests that more space in the mesoporous channels of SBA-15 has been occupied by Ni–B particles, making them inaccessible for nitrogen. Table 1 also shows that the active surface area (S_H) of the supported Ni–B catalysts derived from hydrogen chemisorption decreases in the order of Ni–B/SBA-15 > Ni–B/SiO_2 > Ni–B/MCM-41 > Ni–B/HMS, which does not follow the BET surface areas of the catalysts, but in line with the porosity of the original supports.

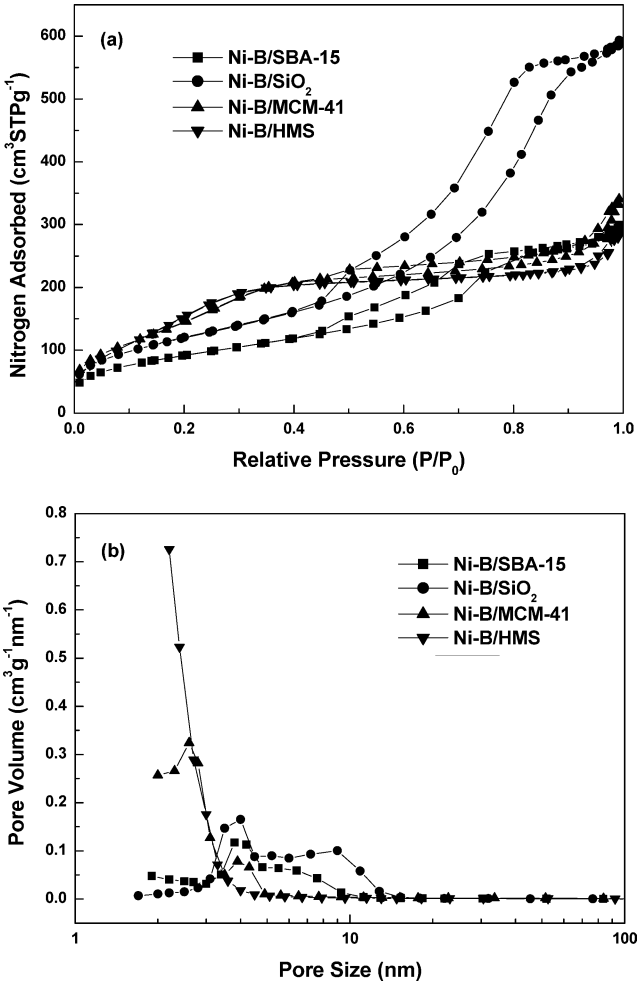

Fig. 2. Nitrogen adsorption–desorption isotherms (a) and pore-size distribution curves calculated by the BJH equation in the desorption branch (b) of Ni–B/SBA-15, Ni–B/MCM-41, Ni–B/HMS, and Ni–B/SiO_2.

On the other hand, although the preparation condition for all catalysts remained the same, the compositions of the Ni–B alloys obviously deviate from each other over different supports. It seems that the characteristic texture of the mesoporous silicas can affect the nature of the Ni–B parti-

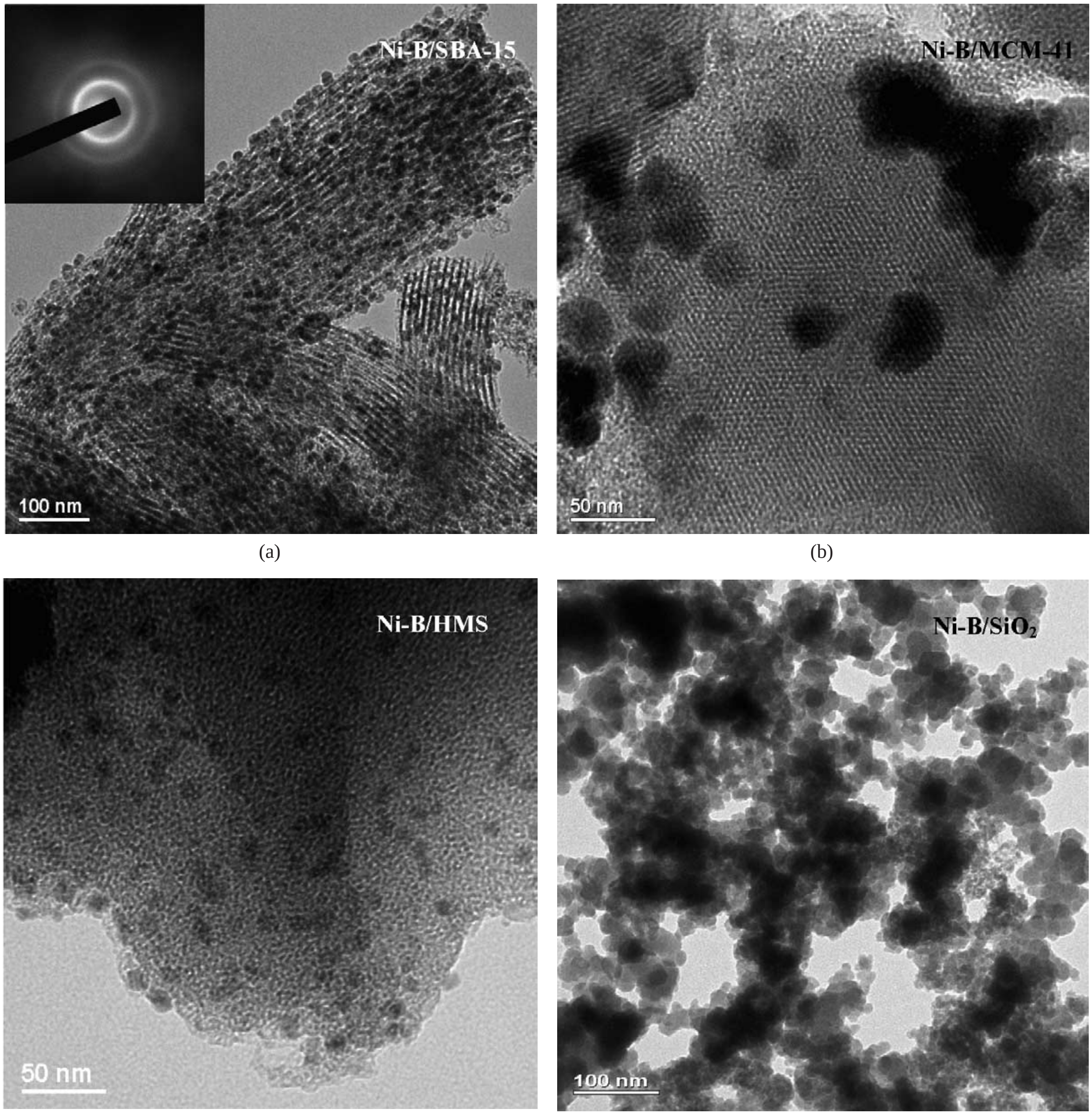

(a) (b)

(c) (d)

Fig. 3. TEM images of (a) Ni–B/SBA-15, (b) Ni–B/MCM-41, (c) Ni–B/HMS, and (d) Ni–B/SiO$_2$ samples. Inset in (a) is the SAED pattern of the Ni–B particles.

cles by providing pores with different structures in which the reduction of the nickel ions by borohydride occurs.

3.2. *Size and location of the Ni–B particles*

The above nitrogen adsorption results indicate the blockage of the pores of the mesoporous silicas by supported Ni–B; however, they cannot discriminate the situations if it is due to covering the external surface or entering the channels of the support. The TEM micrograph shown in Fig. 3a reveals that the Ni–B particles (with darker contrast as confirmed by EDX) are located in the SBA-15 channels, whereas for Ni–B/MCM-41 and Ni–B/HMS, Fig. 3b and 3c, respectively, the Ni–B particles are mainly situated on the outer surface of the supports. For Ni–B/SiO$_2$, since the channels of commercial SiO$_2$ are irregularly connected and the pore sizes are broadly distributed, it is not easy to identify the position of the Ni–B particles from Fig. 3d. However, by analogy to the cases of SBA-15 with large pores and MCM-41 and HMS with small pores, it is safe to assume that a portion of Ni–B particles are in the interior of the large pores of commercial SiO$_2$, while others are on the exterior of the support. Furthermore, on the basis of the relatively limited decrement of the total pore volume (∼13%) for Ni–B/SiO$_2$, we suggest that the Ni–B particles are dominant on the outer surface.

Fig. 3a as well as Table 1 shows that the particle size of Ni–B (∼6 nm) in Ni–B/SBA-15 is uniform and much smaller than that of the unsupported Ni–B particles (∼35 nm) [9], which is attributed to the confined growth of Ni–B particles in the channels of the mesoporous SBA-15. For Ni–B/MCM-41 and Ni–B/SiO_2 catalysts, the Ni–B particles are agglomerated and dispersed in size. As for Ni–B/HMS, although without the confinement of the channels, the Ni–B particles on the surface are small (∼15 nm) and homogeneously distributed, suggesting the existence of some interaction between Ni–B particles and HMS support. Moreover, SAED patterns of the Ni–B particles on all four catalysts exhibit only diffuse Debye rings rather than distinct dots, verifying the amorphous nature of the Ni–B particles (inset in Fig. 3a) [26].

The TEM characterization clearly demonstrates that the texture of the mesoporous silicas plays a more complicated role than only influencing the particle size of the supported species. The present study manifests that the particle size of the supported species is not straightforwardly related to the pore size of the support, and the location of the particles can be quite different over different mesoporous materials. So it can be misleading if only using X-ray line broadening to interpret the influence of support pore size on the particle size of the supported species [25].

As to the different sizes and locations of the Ni–B particles over regular mesoporous silicas, we tentatively attribute it to the unique feature of the reductant-impregnation method and the different textures of the mesoporous materials. After reductant-impregnation, the pores of the mesoporous silicas were filled with KBH_4 solution. After the addition of $NiCl_2$ solution, the deposition of Ni–B occurred in the channels accompanied by the release of hydrogen [7]. As the mesopores in SBA-15 are interconnected by micropores [17], hydrogen is anticipated to leave the interior of SBA-15 more easily, while its dissipation in the mesopores of MCM-41 and HMS was blocked by the formed Ni–B particles. Thus the Ni–B particles were pushed out by hydrogen and aggregated on the external surfaces of MCM-41 and HMS. On the other hand, it is also possible that the dimension of the Ni–B particles cannot be reduced further due to the inherent limitation of the preparation method, leading to Ni–B particles being too large for the mesopores of MCM-41 and HMS to accommodate them.

3.3. Thermal stability

The small-angle XRD patterns of SBA-15, KBH_4/SBA-15, and Ni–B/SBA-15 are given in Fig. 4a. The well-resolved (100), (110), and (200) diffraction peaks suggest the preservation of the regular mesoporous structure of SBA-15 during catalyst preparation and in the final Ni–B/SBA-15 catalyst, corroborating well with the TEM result in Fig. 3a.

Fig. 4b is the large-angle hot-stage XRD patterns of Ni–B/SBA-15 at different temperatures. At ambient temperature no diffraction peak was observed, confirming that the amorphous Ni–B particles are highly dispersed on SBA-15. Similar results have been reported by Wang et al. [27] who did not find any diffraction peaks in calcined Co/SBA-15 with Co loading up to 20 wt%. When the temperature was elevated to 473 K, a broad peak centered at 2θ of ∼45° appeared due to the occurrence of nucleation [26]. For unsupported amorphous Ni–B catalyst, aside from the peak at ∼45°, Yamashita et al. [28] and Li et al. [12] observed additional small features owing to Ni_2B and Ni_3B phases. In the present case, because of the large BET surface area of SBA-15, the high dispersion of these phases makes them indiscernible by XRD. When the Ni–B/SBA-15 catalyst was further heated to 523 K, various crystalline diffraction peaks at 2θ of 44.2, 51.5, and 76.1° were developed, which are attributed to metallic Ni(111), (200), and (222) planes, respectively [29]. The Ni crystallites at that temperature are small considering the broad width of the diffraction peaks. At 873 K, the growth of the Ni crystallites led to stronger and narrower diffraction peaks. For other supported Ni–B catalysts, their crystallization processes are similar to that of Ni–B/SBA-15 and thus are not displayed here again.

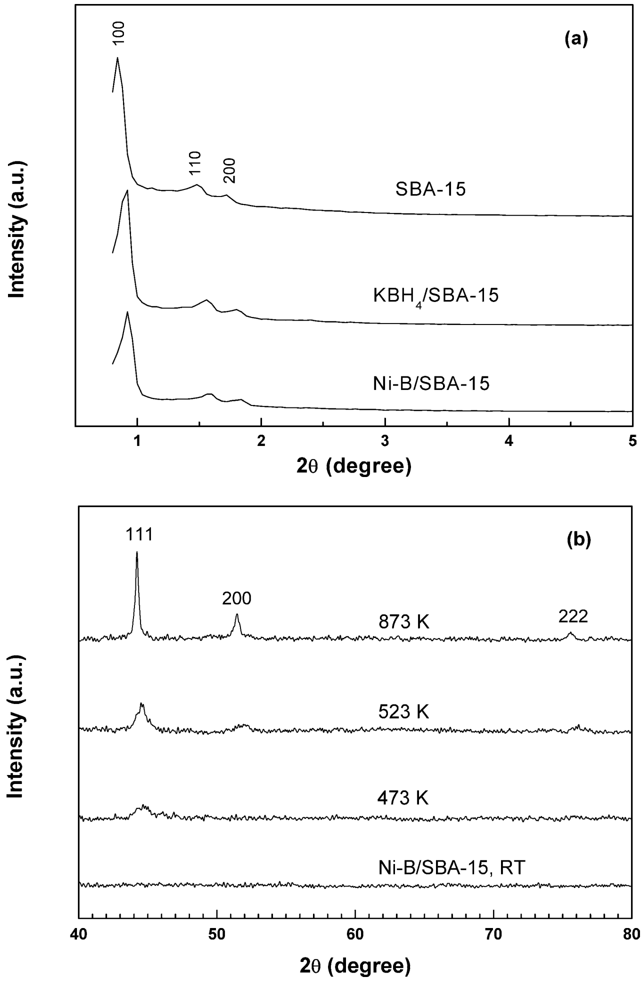

Fig. 4. (a) Small-angle XRD patterns of original SBA-15, KBH_4/SBA-15, and Ni–B/SBA-15, and (b) hot-stage XRD patterns of Ni–B/SBA-15 catalyst treated at different temperatures.

3.4. Surface species and chemical states

As the XPS spectra of the mesoporous silica-supported Ni–B catalysts are similar, in Fig. 5 only the XPS spectra of Ni–B/SBA-15 are illustrated as a representative. From Fig. 5a, one can see that almost all the nickel species in Ni–B/SBA-15 are in their elemental state with the BE of the Ni $2p_{3/2}$ level at 853.0 eV [30]. In Fig. 5b, besides elemental B with its 1s level at ∼188.2 eV, oxidized boron is identified on Ni–B/SBA-15 with B 1s level at ∼193.1 eV [30], which is due to the hydrolysis of BH_4^- during the reduction process being inevitable for a reaction carried out in aqueous solution [7].

Note that although no significant BE shift of metallic nickel is observed, the BE of elemental boron in Ni–B shifts about +1.1 eV relative to pure boron [30]. Based on XPS measurements, Okamoto et al. claimed that in amorphous Ni–B alloy boron donates electrons to the alloying nickel [31,32], so boron is electron deficient while nickel is electron rich. Our previous DFT calculation employing the Ni_mB_2 ($m = 1$–4) cluster model also supported their observation [33]. The electronically modified Ni species is anticipated to display catalytic properties different from pure Ni, such as Raney Ni.

3.5. eAQ selective hydrogenation

The percentage yield of H_2O_2 (X) over the mesoporous silica-supported Ni–B catalysts as a function of reaction time is plotted in Fig. 6. For comparison, the percentage yield of H_2O_2 on routine Raney Ni catalyst is also presented. As shown in Fig. 6, on these supported Ni–B catalysts, the yield of H_2O_2 increased steeply to ∼100% and then declined very slowly. In contrast, on Raney Ni catalysts the yield of H_2O_2 reached 67% and then dropped very quickly. The reaction time corresponding to the maximum yield of H_2O_2 and the TOF values are summarized in Table 2. The activities of the supported Ni–B catalysts are in the sequence of Ni–B/SBA-15 > Ni–B/SiO$_2$ > Ni–B/MCM-41 > Ni–B/HMS.

According to Scheme 1, the percentage yield of H_2O_2 only reflects the overall hydrogenation selectivity to $eAQH_2$ and H_4eAQH_2. In order to have a deep insight into the difference in the catalytic behavior of these catalysts, we monitored the evolutions of eAQ and H_4eAQ during the hydrogenation process. It should be stressed again that eAQ

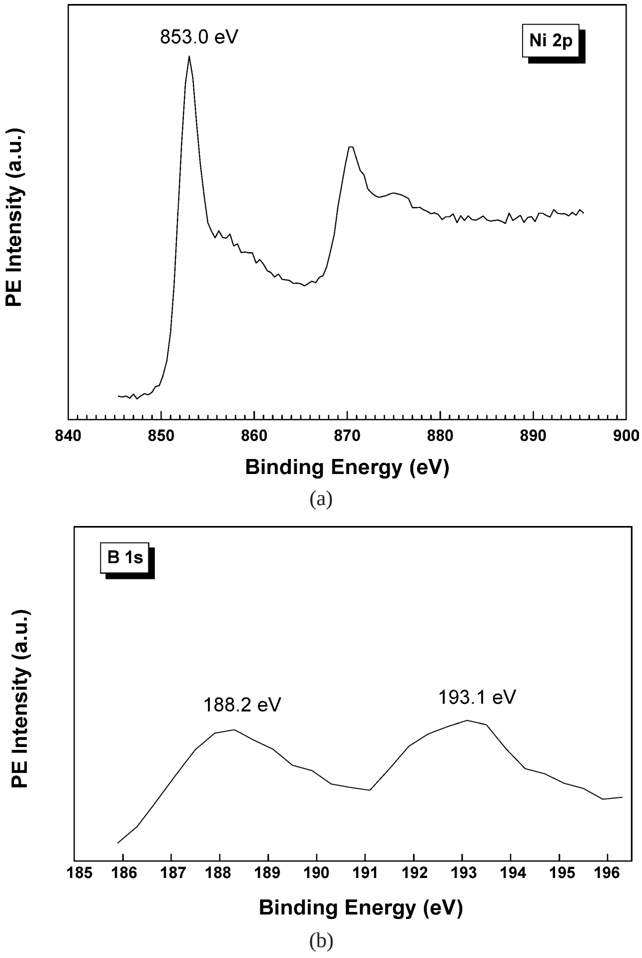

(a)

(b)

Fig. 5. XPS spectra of Ni 2p (a) and B 1s (b) levels of Ni–B/SBA-15 catalysts.

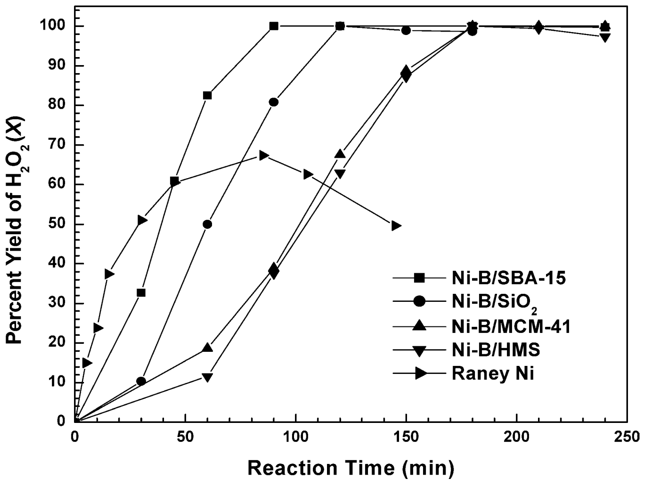

Fig. 6. The percentage yield of H_2O_2 (X) over the mesoporous silica-supported Ni–B catalysts and Raney Ni as a function of reaction time. (Reaction conditions: [eAQ] $= 50$ g l^{-1}, $T = 323$ K, $P_{H_2} = 0.3$ MPa, $r_s = 1000$ rpm, $W_{cat} = 1.0$ g.)

Table 2
The catalytic behavior of the mesoporous silica-supported Ni–B catalysts in eAQ selective hydrogenation

Catalyst	$X_{H_2O_2}$[a] (%)	t[a] (min)	$Y_{H_4eAQH_2}$[a] (mol%)	TOF (s^{-1})
Ni–B/SiO$_2$	100	120	7.2	0.08
Ni–B/HMS	100	180	2.5	0.03
Ni–B/MCM-41	100	180	4.3	0.05
Ni–B/SBA-15	100	90	0	0.12
Raney Ni	67.3	85	52.7	0.60

[a] The maximum yield of H_2O_2 ($X_{H_2O_2}$) and the corresponding reaction time (t) and H_4eAQH_2 yield ($Y_{H_4eAQH_2}$).

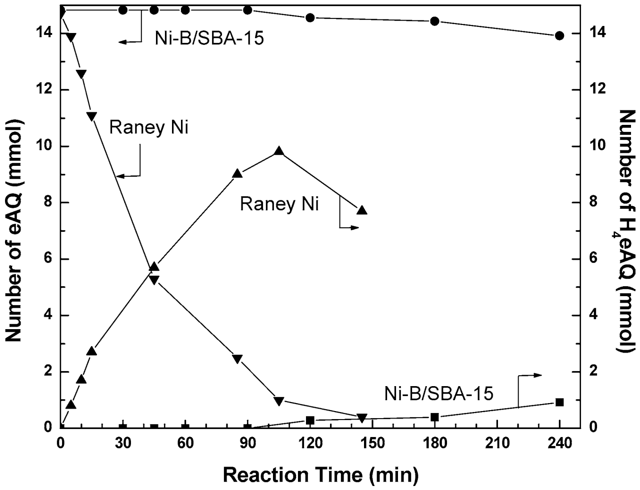

Fig. 7. The evolutions of eAQ and H_4eAQ over Ni–B/SBA-15 catalyst and Raney Ni as a function of reaction time. (Reaction conditions: [eAQ] = 50 g l^{-1}, $T = 323$ K, $P_{H_2} = 0.3$ MPa, $r_s = 1000$ rpm, $W_{cat} =$ 1.0 g.)

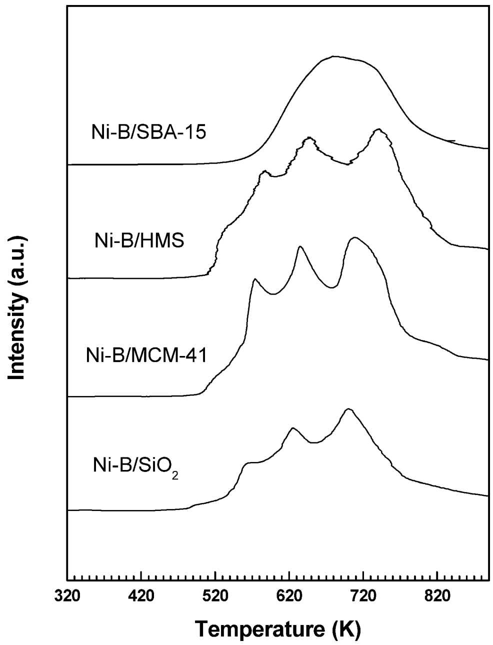

Fig. 8. H_2-TPD profiles of the mesoporous silica-supported Ni–B catalysts.

virtually denotes the sum of $eAQH_2$ and unreacted eAQ, while H_4eAQ is equal to H_4eAQH_2 in quantity.

Table 2 and Fig. 7 show that over Raney Ni catalysts, H_4eAQH_2 was produced as soon as the hydrogenation commenced. At the maximum yield of H_2O_2, 52.7 mol% of eAQ has been converted to H_4eAQH_2, implying that Raney Ni is not selective in carbonyl group hydrogenation. Further reaction led to the formation of some degradation products such as H_8eAQH_2 as verified by GC-MS analysis, thus decreasing the yield of H_2O_2. Over mesoporous silica-supported Ni–B catalysts, the yield of H_4eAQH_2 decreases in the sequence of Ni–B/SiO_2 > Ni–B/MCM-41 > Ni–B/HMS > Ni–B/SBA-15 when reaching the maximum yield of H_2O_2. However, even on the least selective Ni–B/SiO_2 catalyst, the yield of H_4eAQH_2 is only 7.2 mol%, showing the superior selectivity of the amorphous Ni–B catalysts to Raney Ni catalyst in carbonyl group hydrogenation, supposedly relating to the unique electronic property of Ni modified by B as revealed by XPS. By analogy, the deviation in the electronic property of the amorphous Ni–B catalysts, as a consequence of their different composition, may also contribute to the different activity and selectivity in eAQ selective hydrogenation.

It is worth noting that on Ni–B/SBA-15, $eAQH_2$ is the only product when H_2O_2 yield achieves 100%. This demonstrates that over the Ni–B/SBA-15 catalyst, the carbonyl group is preferentially hydrogenated, while hydrogenation of the aromatic ring does not occur unless all the carbonyl groups are saturated. Fig. 7 shows that a prolonged reaction period led to a decrease in the amount of $eAQH_2$ and simultaneously an increase in H_4eAQH_2. However, even after a reaction time of 240 min, the amount of eAQ only dropped by 6%, meanwhile no degradation products appeared, further signifying the excellent selectivity of the Ni–B/SBA-15 catalyst, which is consistent with TEM characterization pointing to a more uniform distribution and population of the Ni–B active component when using SBA-15 as the support. The better structural uniformity of the Ni–B particles in Ni–B/SBA-15 is further revealed by H_2-TPD profiles displayed in Fig. 8. As shown in Fig. 8, for Ni–B/MCM-41, Ni–B/HMS, and Ni–B/SiO_2 catalysts, they all exhibit three desorption peaks, implying that there are at least three types of adsorption sites on these catalysts. For comparison, although the hydrogen desorption peak of Ni–B/SBA-15 is too broad to be simply attributed to a single peak, it is much narrower than the desorption profiles of other samples. This points to the fact that a wider distribution not only in particle size but also in other particle properties such as structural short-range ordering of the amorphous Ni–B clusters in other catalysts is a likely cause for their inferior catalytic performance.

4. Conclusion

The combination of the physicochemical techniques leads to a clear view on the nature of the mesoporous silica-supported amorphous Ni–B catalysts. The composition, size, and location of the supported Ni–B particles are profoundly influenced by the pore structure of the mesoporous silicas. The confinement of the pores or the strong interaction between Ni–B particles and support leads to highly dispersed uniform Ni–B nanoparticles using SBA-15 and HMS as support. In the liquid-phase hydrogenation of eAQ to $eAQH_2$, Ni–B catalysts supported on regular mesoporous silica exhibit better selectivity than on irregularly pore-structured commercial SiO_2. The superior activity and exclusive selectivity are obtained on Ni–B/SBA-15, which is attributed to the predominant population of the size-specific Ni–B particles having more uniform microstructure within the SBA-15 channels.

Acknowledgments

This work is supported by the State Key Basic Research Development Program (G2000048009 and 2003CB615807), the NSF of China (20203004 and 20005310), and Shanghai Science and Technology Committee (03QB14004).

References

[1] C.S. Cronan, Chem. Eng. 6 (1959) 118.
[2] T. Ulmann (Ed.), Encyclopedia of Industrial Chemistry, vol. A3, VCH, Weinheim, 1989, p. 443.
[3] J.I. Kroschwitz, M. Howe-Grant (Eds.), Kirk-Othmer Encyclopedia of Chemical Technology, vol. 13, fourth ed., Wiley, New York, 1995, p. 961.
[4] A. Drelinkiewicz, M. Hasik, M. Kloc, Catal. Lett. 64 (2000) 41.
[5] A. Drelinkiewicz, J. Mol. Catal. 101 (1995) 61.
[6] E. Santacesaria, M. Di Serio, R. Velotti, U. Leone, J. Mol. Catal. 94 (1994) 37.
[7] Y. Chen, Catal. Today 44 (1998) 3.
[8] Á. Molnár, G.V. Smith, M. Bartók, Adv. Catal. 36 (1989) 329.
[9] J.F. Deng, J. Yang, S.S. Sheng, H.G. Chen, G.X. Xiong, J. Catal. 150 (1994) 434.
[10] H.X. Li, W.J. Wang, H. Li, J.F. Deng, J. Catal. 194 (2000) 211.
[11] Z. Liu, S.H. Xie, B. Liu, J.F. Deng, New J. Chem. 23 (1999) 1057.
[12] H. Li, H.X. Li, J.F. Deng, Catal. Today 74 (2002) 53.
[13] R.B. Zhang, F.Y. Li, Q.J. Shi, L.T. Luo, Appl. Catal. A 205 (2001) 279.
[14] S.T. Wong, J.F. Lee, J.M. Chen, C.Y. Mou, J. Mol. Catal. A 165 (2001) 159.
[15] A. Corma, Chem. Rev. 97 (1997) 2373.
[16] X.Y. Chen, H.R. Hu, B. Liu, M.H. Qiao, K.N. Fan, H.Y. He, J. Catal. 220 (2003) 254.
[17] D.Y. Zhao, J.L. Feng, Q.S. Huo, N. Melosh, G.H. Fredrickson, B.F. Chmelka, G.D. Stucky, Science 279 (1998) 548.
[18] M. Grun, K.K. Unger, A. Matsumoto, Micropor. Mesopor. Mater. 27 (1999) 207.
[19] P.T. Tanev, M. Chibwe, J. Pinnavaia, Nature 368 (1994) 321.
[20] E.P. Barrett, L.G. Joyner, P.P. Halenda, J. Am. Chem. Soc. 73 (1951) 373.
[21] C.H. Bartholomew, R.B. Pannell, J. Catal. 65 (1980) 390.
[22] K.S.W. Sing, D.H. Everett, R.A.W. Haul, L. Moscou, R.A. Pierotti, J. Rouquérol, T. Siemieniewska, Pure Appl. Chem. 57 (1985) 603.
[23] Z.H. Luan, M. Hartmann, D.Y. Zhao, W.Z. Zhou, L. Kevan, Chem. Mater. 11 (1999) 1621.
[24] S.J. Gregg, K.S.W. Sing, Adsorption, Surface Area and Porosity, second ed., Academic Press, New York, 1982.
[25] A.Y. Khodakov, A. Griboval-Constant, R. Bechara, V.L. Zholobenko, J. Catal. 206 (2002) 230.
[26] T. Osaka, K. Arai, N. Masubuchi, Y. Yamazaki, T. Namikawa, Jpn. J. Appl. Phys. 28 (1989) 866.
[27] Y. Wang, M. Noguchi, Y. Takahashi, Y. Ohtsuka, Catal. Today 68 (2001) 3.
[28] H. Yamashita, M. Yoshikawa, T. Funabiki, S. Yoshida, J. Chem. Soc., Faraday Trans. 1 82 (1986) 1771.
[29] S.D. Robertson, J. Freel, R.B. Anderson, J. Catal. 24 (1971) 130.
[30] Handbook of X-ray Photoelectron Spectroscopy, Perkin-Elmer Corporation, 1992.
[31] Y. Okamoto, Y. Nitta, T. Imanaka, S. Teranishi, J. Chem. Soc., Faraday Trans. 1 15 (1979) 2027.
[32] Y. Okamoto, Y. Nitta, T. Imanaka, S. Teranishi, J. Catal. 64 (1980) 397.
[33] Z.G. Fang, B.R. Shen, J. Lu, K.N. Fan, J.F. Deng, Acta Chim. Sinica 57 (1999) 894.